Seeding-free inlet flow distortion measurements using filtered Rayleigh scattering: integration in a complex intake test facility

Matteo Migliorini[1], Pavlos K Zachos[2], David G MacManus[3],
School of Aerospace, Transport and Manufacturing, Cranfield University, Bedfordshire, MK43 0AL, UK

Ulrich Doll[4],
Experimental Thermal Hydraulics Group, Paul Scherrer Institute, Forschungstrasse 111, Villigen PSI, 5232, Switzerland

Michael Dues[5], Jonas Steinbock[6], Fritz Dues[7], Adi Siswanto[8],
ILA R&D GmbH, Rudolf-Schulten-Straße 3, Jülich, 52428, Germany

Sergey M Melnikov[9], Ingo Röhle[10].
Berliner Hochschule für Technik, Luxemburger Str. 10, Berlin, 13353, Germany

Highly integrated propulsion systems to achieve fuel savings and reduction of emissions in future aircrafts call for new measurement methods to assess inlet conditions at the engine fan face. Propulsion systems are expected to operate at higher levels of total pressure, total temperature, and swirl distortion due to flow interaction with aerodynamic surfaces and inherent flow distortion within convoluted intakes. Filtered Rayleigh Scattering (FRS) offers capability to assess all these quantities at once, and without the need of seeding particles which cannot be used for in-flight measurements. This paper aims at increasing the technology readiness level of this measurement technique through the application on a lab-scale S-duct diffuser tests and benchmark against Stereo-Particle Image Velocimetry (S-PIV) measurements. Methods to improve the optical integration and mitigate the effect of varying background conditions are hereby explored. Overall, this represents a step forward in the use of FRS as a turnkey solution for the testing and development phase of future propulsion systems.

1 Senior Research Fellow, AIAA member.
2 Reader, AIAA Member.
3 Professor, AIAA Member.
[4] Assistant Professor.
[5] Managing Director.
[6] Researcher.
[7] Student Research Assistant.
[8] Researcher.
[9] Research Associate.
[10] Professor.

I. Introduction

In the last two decades, the aero community has been focused on the development of novel aircraft configurations and propulsion systems to increase flight efficiency and reduce the environmental impact [1]. While great efforts are dedicated to the development of sustainable alternative fuels (SAF) such as e-fuels or hydrogen [2,3], it has been shown that changes in aircraft architecture to integrate propulsion systems more closely to the fuselage can also produce great benefits due to the reduction in the frontal area drag and re-energization of the boundary layer flow [4,5]. These concepts are also well suited to host hybrid-electric propulsion systems [6]. However, the integration of the propulsion systems introduces new challenges to engine operability and reliability. In these anticipated configurations, engines are likely to be presented with increased levels of total pressure and swirl distortion due to the interactions of the inlet flow with aerodynamic surfaces and the effects of the inherent distortion of convoluted diffusers [7,8]. This highlights the need of methods to measure and characterize the flow distortion to de-risk the development of these new propulsion architectures.

In contrast to conventional methods based on pressure based single and multi-hole probes, laser-based flow diagnostics have shown great potential for non-intrusive and synchronous measurements across the plane of the inlet flow distortion with a much finer spatial resolution and with the capability to resolve the unsteady fluctuations [9]. Within this context, Particle Image Velocimetry (PIV) [10–13] and Doppler Global Velocimetry (DGV) [14], have been successfully used to characterize swirl distortions and results have been used for fundamental analysis on the topology, flow modes and spectral distribution of the unsteady swirling flow. Although it is possible to derive the pressure field from the 3D velocity data with relatively good accuracy [15], these techniques cannot measure directly other quantities and rely on the use of seeding particles which may not be applicable to all test environments. A way to address these pitfalls would be the development of more advanced measurement methods with the ability to synchronously capture multiple types of flow distortion, namely total pressure, total temperature and swirl [16,17]. This capability is offered by Filtered Rayleigh Scattering (FRS), which is a non-intrusive, laser-based flow measurement method able to provide simultaneous measurements of velocity, pressure, and temperature across a plane with high spatial resolution and without the requirement to inject seeding particles into the flow [18–20]. As such, it is a promising candidate for the characterisation of the complex, distorted flows in novel aircraft air induction systems not only at ground level test facilities but also at in-flight tests [9].

A new FRS measurement system with the ability to simultaneously measure time-averaged and unsteady three-component velocity, static pressure and temperature fields with high spatial resolution was recently presented [21]. In continuation with the works carried out with a simplified test configuration [22,23], this paper presents the application of the FRS method at the Cranfield Complex Intake Test Facility (CCITF), to characterize complex flow fields at the exit of complex subsonic diffusers pertinent to novel aircraft intake systems. The application aims to demonstrate the FRS method at Technology Readiness Level (TRL) 4. The current work addresses aspects around the integration of the optical system, data acquisition and data processing. This contributes to the further development of this technique for advanced, non-intrusive experimental measurements and a step forward in the path to a higher TRL.

II. Experimental test configuration

The development of novel propulsion systems which are closely coupled with the aircraft is likely to require the use of convoluted air intakes. Previous research demonstrated that these intakes generate complex unsteady flow distortions, which are produced either inherently in the intake or due to onset conditions such as boundary layer ingestion [9,24,25]. The CCITF is developed to reproduce these conditions. A rendering of the facility is shown in Figure 1. The air is drawn into the rig from a bell mouth opening and then flows through a set of straighteners to homogenise the flow. The air then flows through a conditioning section which can be used to reproduce non-uniform inlet conditions of e.g. BLI aircraft, cross-wind or vortex ingestion [24]. A nozzle then reduces the crossflow area to the dimensions of the inlet of the complex diffuser and a cylindrical section is installed upstream the diffuser to enable the measurement of the inlet conditions. A series of diffuser geometries can be tested in this facility, including single or multiple offset ducts. However, previous work at Cranfield University assessed a high-offset S-duct geometry and a substantial amount of previous work on this configuration has been published in the peer-reviewed journal literature. This encompasses experimental and computational studies as well as evaluations of steady and unsteady total pressure distortion, swirl distortion, sensitivity to inlet Mach number, as well as the effectiveness of passive and active flow-control methods [10,13,26–30]. Thus, this high-offset S-duct geometry was deemed adequate for demonstrating FRS on complex flows. The key geometry parameters are reported in Figure 1. An optical cylindrical section is coupled downstream of the S-duct diffuser to enable non-intrusive measurements. A flexible coupling is then introduced to reduce the vibrations generated by the prime mover and a diffuser drives the air to the suction fan.
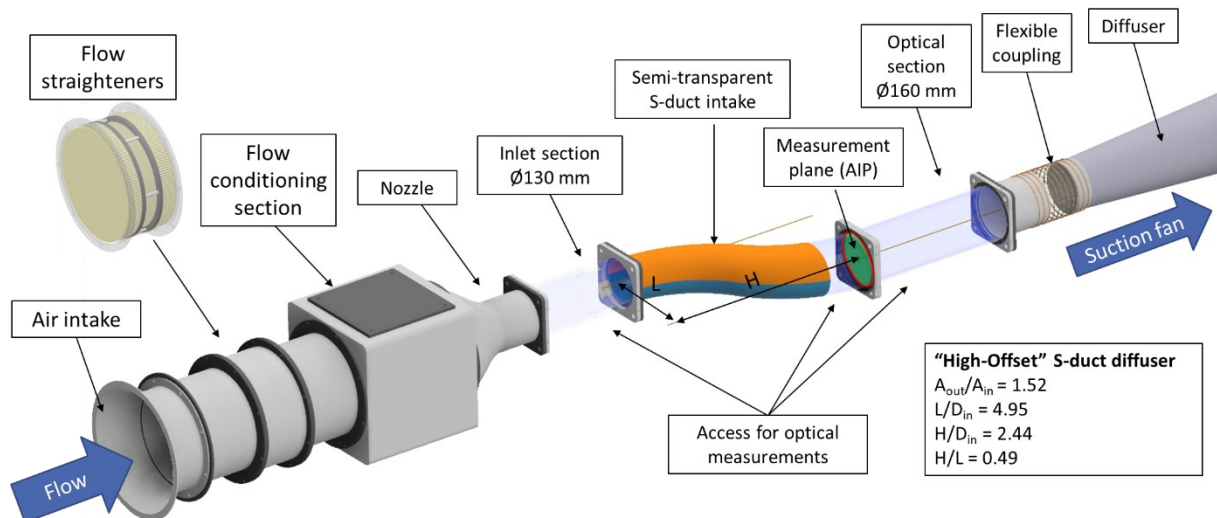
Figure 1: 3D schematic of the Cranfield Complex Intake Test Facility (CCITF) indicating key components.

Subsonic diffuser testing was previously performed at a range of Mach numbers between 0.27-0.60 at the reference inlet plane [13,28]. This corresponds to approximately Mach 0.18-0.38 at the Aerodynamic Interface Plane (AIP) with the selected diffuser geometry. Hence, the required fan power and mass flow rate has been estimated through compressible flow theory by considering previous measurements on the total pressure loss across the S-duct diffuser and suction fan efficiency of 80%. These estimates provided a minimum required fan power of about 23kW and a minimum mass flow rate of 2.8 kg/s (Figure 2). A centrifugal fan above these specifications was selected to be suitable for diffusers which would generate higher pressure losses. The specification of the fan is reported in Figure 3. The centrifugal fan will provide suction to generate the flow distortion at the AIP behind the S-duct for intake tests in a range M_{inlet} = 0.1-0.6. In this configuration, a long optical section downstream of the AIP will provide unrestricted line of sight for testing the intake.
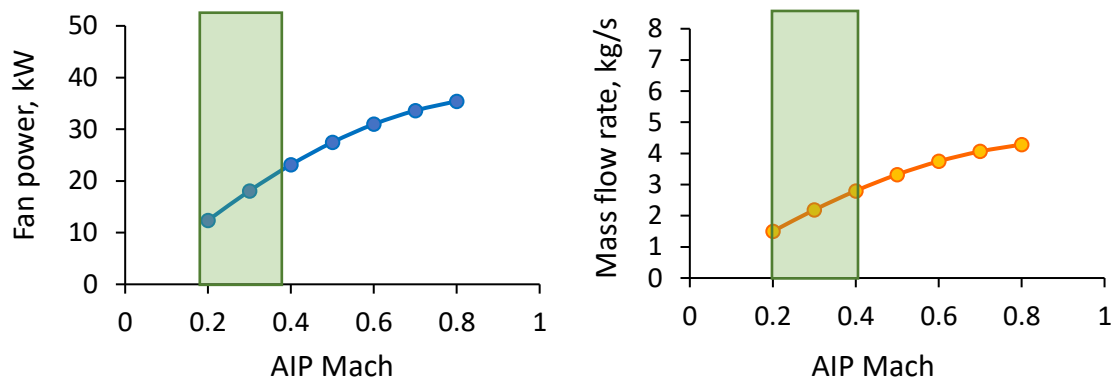
Figure 2: Estimate of the required fan power and mass flow rate for operating the rig in a range of 0.2-0.4 Mach at the AIP.
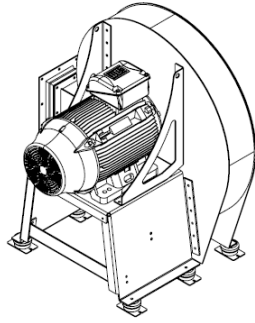
Parameter	Centrifugal fan
Design mass flow rate	4 kg/s
Design static pressure	12 kPa
Fan nominal power	48.6 kW
Motor nominal power	55.0 kW
Motor max speed	2970 rpm

Figure 3: SWSI-BLX-810 by Woodcock & Wilson with key characteristics.

III. FRS measurement system development

A. Multi-property FRS measurements, observation concept and optimization

The combined measurement of time-averaged 3D velocity, temperature and pressure with FRS can be achieved by combining a frequency scanning method with the observation of an area of interest from three different perspectives [31]. Recently, it was demonstrated that this concept can be extended to the measurement of multiple flow quantities based on a single laser wavelength by using additional perspective views, thus enabling time-resolved multi-property measurements by FRS [21,23]. Crucially, this work evidenced that a multi-objective optimization framework can improve the detection sensitivity of the flow variables and it is relevant for both time-averaged and time-resolved design of experiments [21]. This framework allows to determine the optimum detector configuration for a multi-view FRS system, and it was adopted also for the test configuration in the CCITF. The inputs of the framework are the equipment properties, the test rig properties and the scattering geometry (Figure 4, left). The range of the flow quantities expected at the Aerodynamic Interface Plane (Figure 1) have been taken from the available literature of computational and experimental measurements of the S-duct diffuser [10,13,26–30]. By adapting the polar and azimuthal angles α and β, the optimisation tool tries to find an ideal orientation of the six camera perspectives on a spherical surface, so that the standard deviations of the five flow variables become minimal. To obtain these statistical quantities (objectives), Monte-Carlo simulations are conducted based on synthetic FRS data. A key consideration is that due to the expected secondary flows at the AIP, it is beneficial to orient the laser light at a 45° angle relative to the x and y axis (Figure 4, right) as this equalizes the uncertainty in the u and v velocity components [21].
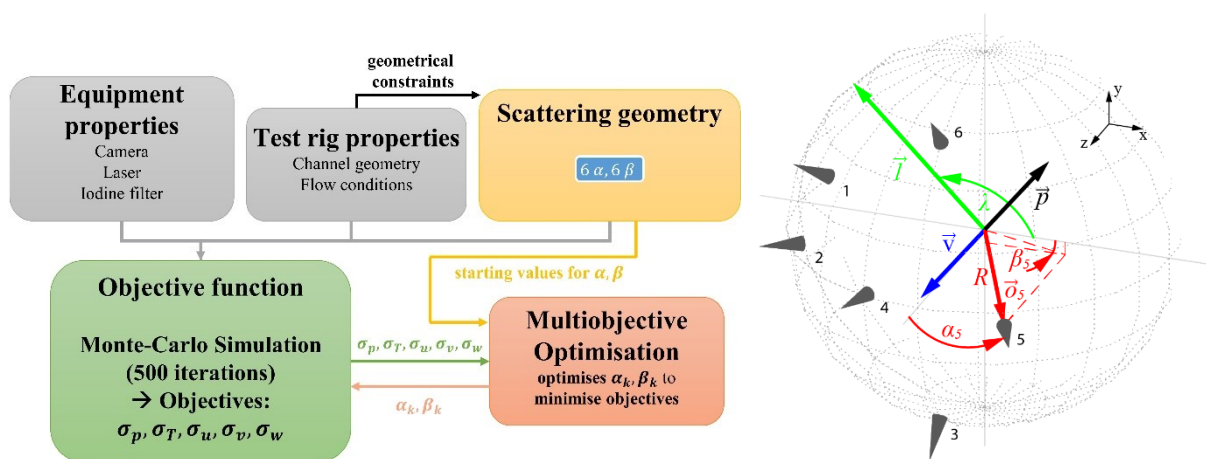

Figure 4: (Left) Multi-objective optimization framework for a multi-view FRS system. (Right) Optimised six-view observation concept with the camera perspectives (grey cones) oriented on a sphere, laser propagation along $\vec{l}$ and flow velocity along $\vec{v}$. $\vec{p}$ denotes the direction of polarisation of the laser light (adapted from [21]).

B. FRS design of experiment and system integration in the CCITF

This section collects the details of the implementation of the FRS measurement system in the CCITF. The objective is to offer a comprehensive view on how the FRS system requirements are met and provide solutions to the application requirements. The system can be subdivided in two main sub-assemblies: the laser hardware and the relative measurement and control system, and the optical imaging hardware. The laser hardware comprises a narrow-linewidth AzurLight continuous-wave fibre laser (CW laser, Figure 5), which produces a 532 nm green laser light at a spectral bandwidth below 200 kHz. The laser power output can be controlled within 0.1 – 6.0 W through an external NKT Photonics ADJUSTIK Y10 seed laser unit. The output frequency is adjusted through either fast piezo tuning if in the range of 10 GHz, or slow thermal turning over 700 GHz. A single mode fibre is used to direct a small portion of the laser light into the wavelength control unit HighFinesse WS-8 (WLM, Figure 5). This is to achieve stability of the laser's output frequency below 1 MHz to the set point. This device is calibrated at any change of environmental conditions to avoid any drift in the frequency measurement by taking as reference the stabilized frequency of a Helium-Neon laser (He-Ne laser, Figure 5). Power output of the CW laser is continuously monitored with a photodiode by using a beamsplitter, a diffusion disk and collecting lenses (Figure 5).
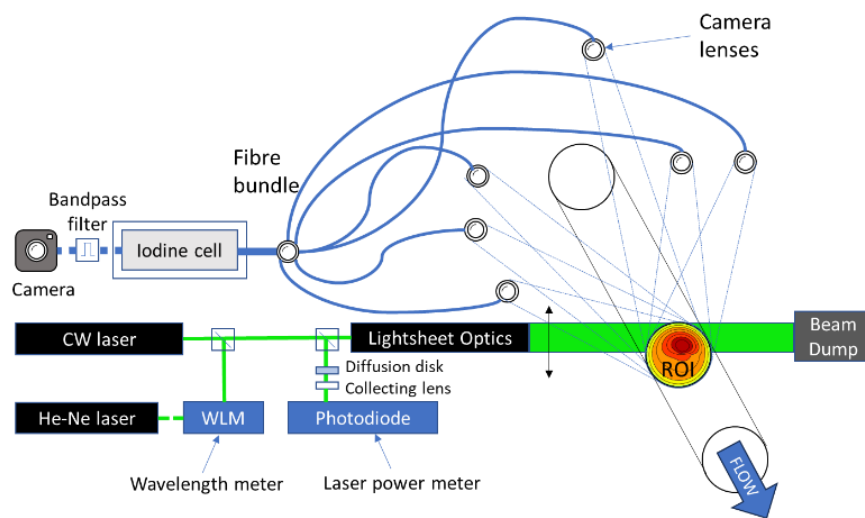

Figure 5: FRS system overview including laser hardware (CW laser and He-Ne reference laser), optical measurement equipment (wavelength and power meter), laser light delivery and imaging arrangement with camera fibre bundle.

The CW laser beam is converted in a laser light sheet through a series of enclosed optics and a spinning prism as shown in Figure 6a. This enables the generation of a lightsheet of approximately 100 mm height, which was reputed adequate for the generation of FRS data with relatively good signal-to-noise ratio. However, this was not sufficient to illuminate the 160 mm diameter region of interest (full AIP, Figure 1). This has been addressed by the acquisition of two separate datasets of the upper and lower portion of the AIP, whose data were successively merged (Figure 6c, d, e). This produced only minor artifacts in the output velocity and pressure distribution, as discussed in section IV. As prescribed from the multi-objective optimization, the laser light was integrated by means of a 45° mount at the $0.144*D_{AIP}$ S-duct outlet plane for parity in the uncertainties of the in-plane velocity components (Figure 6c). Additional steps were taken to reduce the laser light reflections and distortions, which would have been inevitably caused by a cross-plane illumination through a cylindrical glass duct. A bespoke flange coated in matt black has been designed to introduce a 6 mm streamwise gap between the S-duct outlet plane and the optical cylinder downstream walls (Figure 1) to avoid spurious reflections of the laser when illuminating the cylindrical optical domain. This gap has been sealed with side walls at all sides of the flange with rubber gasket interfaces (Figure 6b). O-rings have been embedded to seal the interface between the flange and cylindrical domains upstream and downstream of the flange. Light sheet windows with broadband anti-reflective coating centered at 532nm wavelength provided entry and exit paths for the laser lightsheet through the gap (Figure 6b). A provision for a target plate for the camera calibration was offered through one of the side walls of the flange, which allowed for the calibration procedure to be performed in-situ, without the de-commissioning of the optical domains. This enabled to obtain the FRS scattering signal with only minimal reflections at the peripheral walls of the AIP (Figure 6d, e).
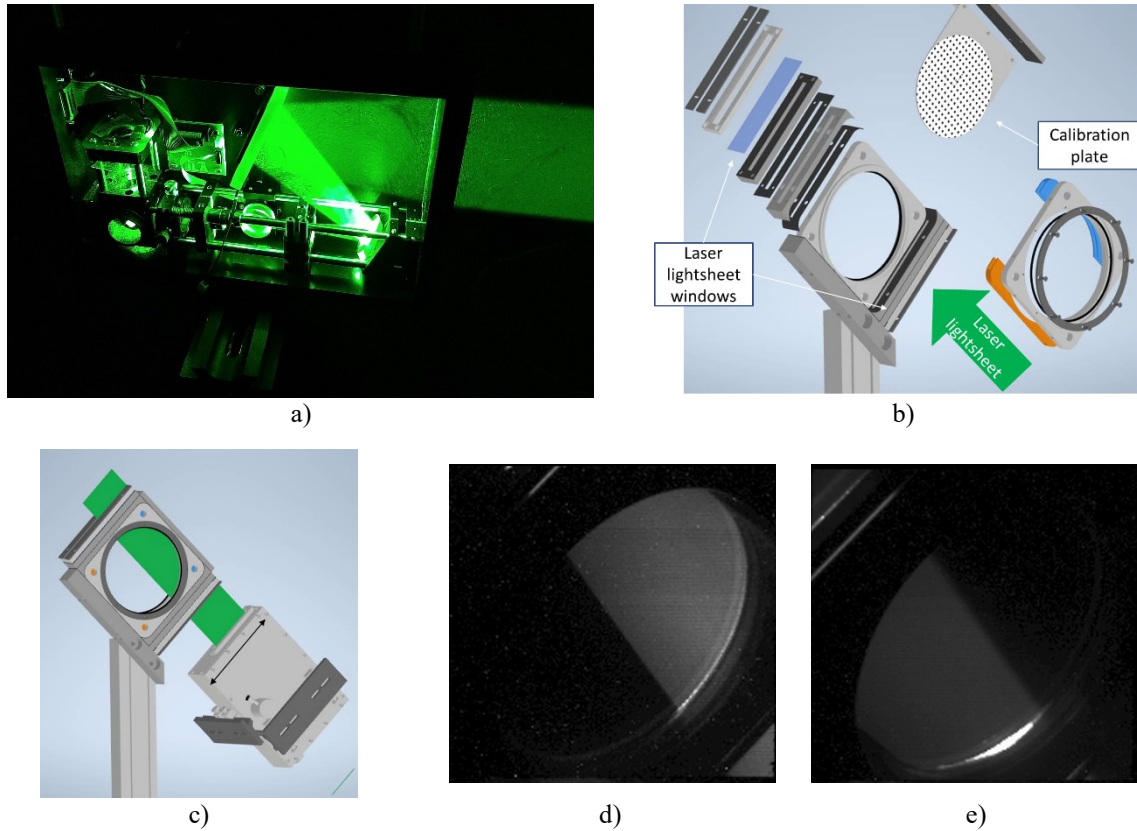
Figure 6: FRS lightsheet delivery: a) CW laser lightsheet optics; b) laser lightsheet for reflections mitigations at the AIP; c) translation of the laser lightsheet to cover full AIP measurements in two takes; and d-e) FRS signal from the two lightsheet positions across the AIP.

The optical imaging hardware consists of a 6-branch image fibre bundle, an iodine cell, a bandpass filter (10 nm FWHM @ 532 nm) and a CMOS camera (PCO Edge 4.2) (Figure 5). Each fibre bundle front end is equipped with camera lenses with f-number 1.4 and a focal length of 16 mm. These lenses collect the light scattered from the measurement plane and focus this on a square light sensitive area of 16 mm^2 which comprises 400 fibres in each direction with 10μm core diameter (Figure 7a, input side). The fibres are leached in a cladding which is insensitive to light (Figure 7c) and thus the light signal is transmitted only through the individual fibres, with a manufacturer specified efficiency of 40%. The fibres from each bundle are coherently and orderly assembled in a single rectangular area of size 12 x 8 mm, so that the views from the six individual fibre bundles are combined into a single one (Figure 7b, output side). The collected light is then transmitted through transfer optics and successively filtered by a molecular filter cell containing vaporized iodine at 80°C. The temperature of the iodine cell was kept constant through a PID controller and additional insulation was provided during the tests to limit the influence of varying environmental conditions on the transmittance characteristics. The transmittance of the iodine cell was calibrated with the average of 10 scans at different wavenumbers with an accuracy below 0.5% (Figure 8).
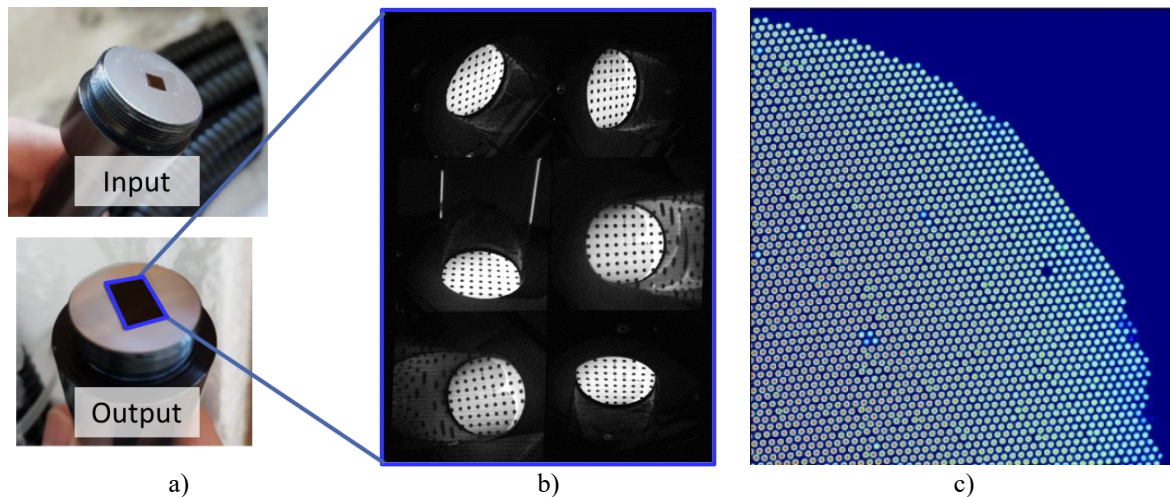
Figure 7: FRS hardware components: a) input and output fibre bundle sensitive areas, b) combined views of the calibration plane in the output fibre end, and c) close-up of the lattice structure of the fibres in the bundle.
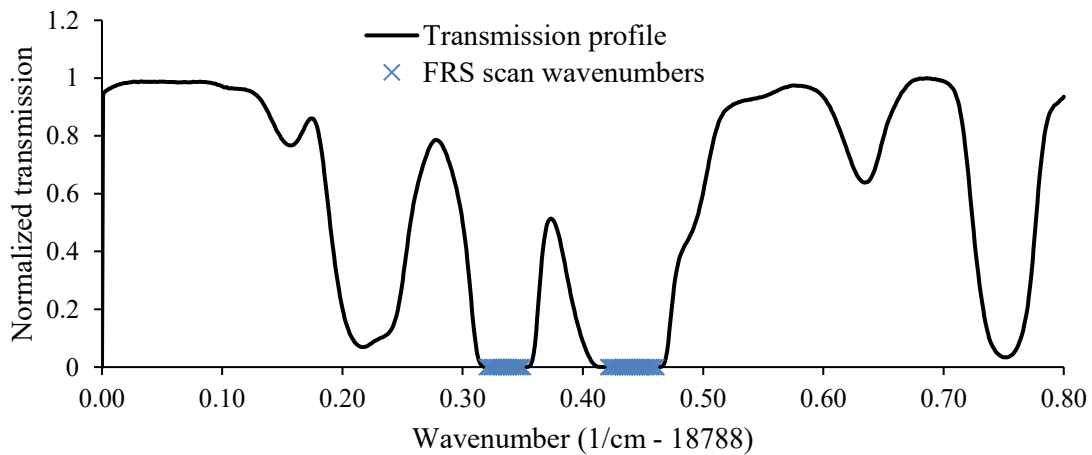

Figure 8: Normalized transmission spectrum of the iodine cell, averaged over 10 measurement repetitions, and indication of the wavenumbers used for the FRS scanning method.

The fibre bundles were located at positions dictated by the optimisation framework of Doll et. al [21], which prescribed the optimum setup for lowest uncertainty of the measured variables. Cameras were placed at points located on a sphere of 540 mm centered at the AIP (Figure 9a). To align the optimised perspectives at the test facility, positions of the cameras were back-projected on a wooden board located downstream of the AIP to obtain directions aligned with the optimised camera angles (Figure 9a, b). Tensioned lead strings were installed through a hole in a plate at the AIP centre and through securing the lead strings with pins on the wooden board. Stand-off distances were measured and marked on the lead strings, and these were used as a guide for alignment of the fibre bundle front ends in the prescribed positions (Figure 9b). Camera lenses were subsequently adjusted manually to fine-tune the line of sights on the calibration plane. The fibre bundle ends were held in place with hydraulic magnetic articulated arms to maintain the perspectives in their respective positions. This alignment method produced errors in the placement of the perspective views below 5°, which is an acceptable level according to previous assessments [21]. After the alignment, the camera positions were calibrated using Python's OpenCV toolbox [32]. All six perspectives then were dewarped and mapped onto a common Cartesian grid, resulting in a spatial resolution of 1 pixel/mm.

As shown in Figure 10a, the optimization framework prescribed an arrangement in which all views beside no. 5 were located either along the vertical axis or offset towards the starboard side of the AIP, which caused the left side of the AIP not to be under line-of-sight of several camera perspectives (Figure 10b). The line of sight of this region was partially obstructed by the laser flange edges which blocked the view of the AIP plane internal to the flange. Nevertheless, overall the arrangement of the perspective views offered a good coverage of the AIP plane,

as a minimum of three views always had optical access to the total cross section and approximately 80% of the area could be seen from all six views (Figure 10b).

A complete FRS dataset finally consist of a reference frequency scan obtained under known thermodynamic conditions and zero flow velocity and the data acquired under flow conditions. For both reference and flow data, a frequency scan consisted of 37 discrete frequencies that were distributed within the blocking regions (transmission $< 10^{-5}$) of the two transmission minima around 18788.4 cm^{-1} in Figure 8. The exposure time for each data image was 20 s. To further increase the signal-to-noise-ratio (SNR), measurements were repeated five times and averaged before further processing.

a)   b)
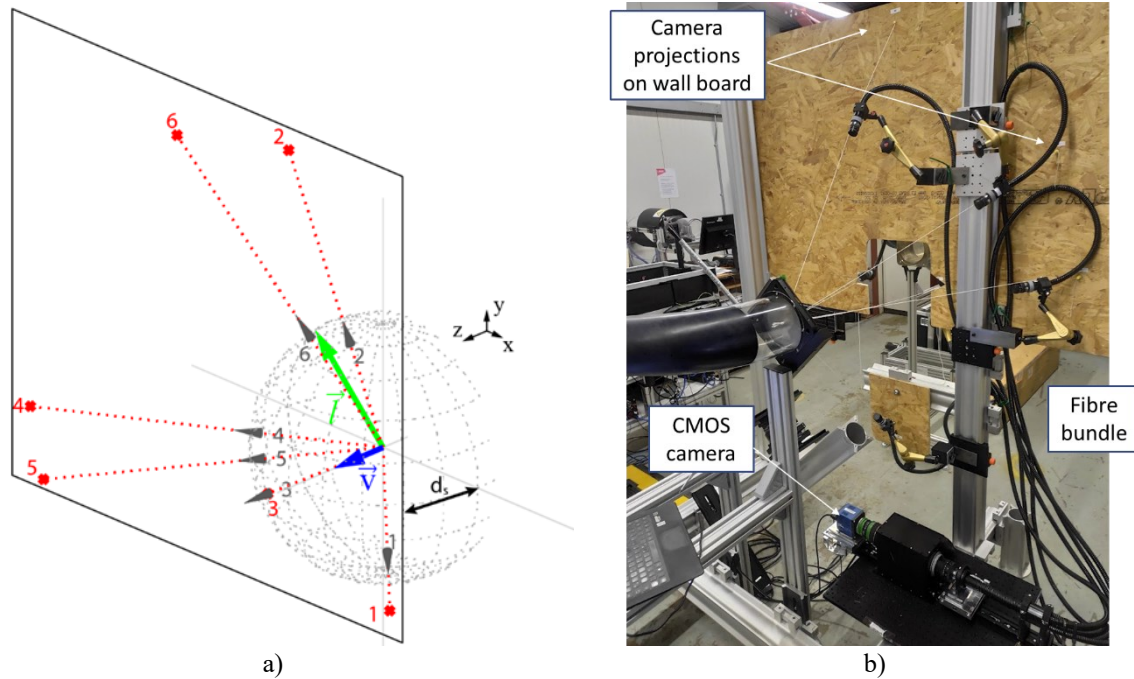
Figure 9: FRS fibre bundle arrangement: a) back projections of camera positions on a plane downstream the AIP, and b) alignment of the camera views through lead strings.

View	x (mm)	y (mm)	z (mm)
1	-386	300	427
2	-526	72	519
3	-88	-462	472
4	-116	-1	675
5	188	-44	613
6	2	601	405

a)   b)
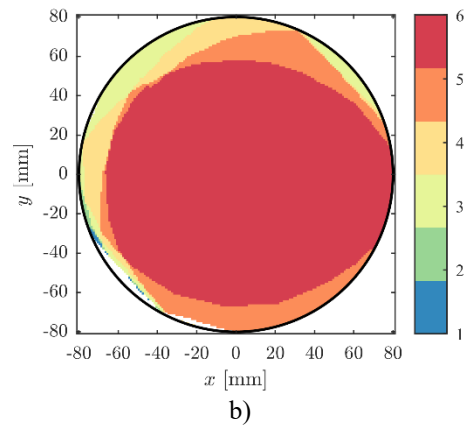
Figure 10: a) Spatial locations of the cameras relative to the centreline of the S-duct AIP plane, and b) coverage of the measurement plane showing the number of overlapping views.

C. FRS data processing and background treatment

The detected signal for a frequency scan at a resolution element of the camera sensor

$$S_{kl} = C_l I_0 \left(f_{kl,\text{FRS}} + B_{kl} \right) \tag{1}$$

can be perceived as a superposition of the FRS intensity $f_{kl,\text{FRS}}$ that carries the flow information, and background intensities B_{kl}, with C as a setup specific constant incorporating e.g. the optical path or the distribution of the laser intensity within the light sheet and I_0 the incident laser power (measured). The index k represents the excitation frequency and l the individual camera perspectives. The FRS signal for a single-component gas flow (air can be treated as such) is [19,20,31,33]

$$f_{kl} = n \sin^2 \phi_{kl} \int_{-\infty}^{\infty} r_{kl} \left(\nu - \nu_{0,k}, p, T, \vec{v}, \theta_{kl} \right) \tau(\nu) \, d\nu, \tag{2}$$

with n the number density (calculated from ideal gas law) and ϕ the angle between observation direction and polarisation. The integral describes a convolution between the Rayleigh scattering's spectral shape r and the iodine filter transmission τ, where ν_0 is the excitation frequency, p the pressure, T the temperature, $\vec{v}$ the 3D velocity vector and θ the angle spanned by observer and laser direction.
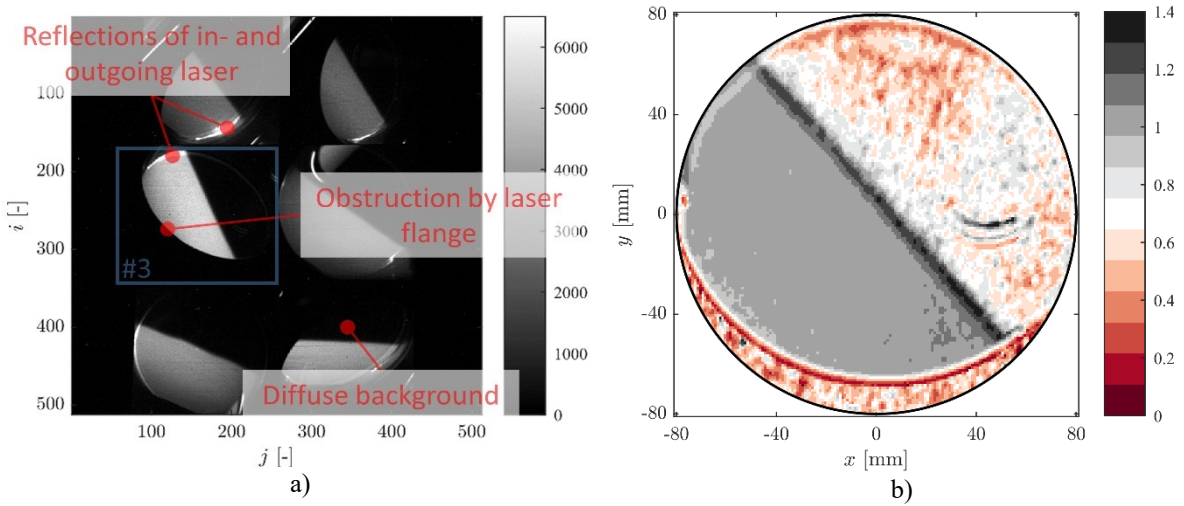
Figure 11: a) Raw FRS image with the light sheet at the lower position. b) Quotient of a dewarped flow and a reference data image for perspective #3 taken at the same excitation frequency. The channel boundaries are indicated by the black solid line.

From Equations (1) and (2) it becomes apparent, that the collected FRS signal not only depends on the five wanted flow variables but also on various experimental parameters that have to be treated. As described in the previous section, the angles ϕ and θ representing the multiple view scattering geometry were obtained from the camera calibration. The setup specific constant C and the background intensity B are typically determined from the reference frequency scan and then used in the evaluation of the flow data. This procedure inherently assumes that C and B remain constant between reference and flow measurement, which works well for simple flow configurations [23] but may cause complications at complex experimental facilities such as the CCITF. Indeed, slight movements of the rig during operation and flow induced vibrations cause the experimental constant as well as the background conditions to change. Several areas that are prone to introduce related errors are highlighted in Figure 11a. When the duct is moving relative to the light sheet, the intensities of the reflections of the incoming and outgoing laser light are going to change. This leads to different background intensities locally in the affected areas, but also to changes in the overall background level caused by the diffuse illumination of the duct walls.

The effect the varying background level between reference and flow measurement has on the FRS data is visualised in Figure 11b. The image shows the ratio of a flow and a reference data frame acquired at the same excitation frequency. The grey area is the region covered by the light sheet and contains the FRS signal. The area above the diagonal consists of the diffuse laser background. While there is little relative change in the light sheet area, a strong variation of the diffuse background can be observed in the non-illuminated region, which can be considered as representative of what is happening behind the light sheet. Moreover, the relative movement of the test rig causes a circular artefact to appear on the lower side, which is attributed to the obstruction of the field of view by the laser flange. To tackle the related detrimental effects on the FRS results, a more robust formulation

of Equation (1) is selected for the data processing. By normalising the detected signal S with its ensemble average over all scanning frequencies [34]

$$Q_{kl} = \frac{S_{kl}}{\langle S_{kl} \rangle_k} = \frac{n \sin^2 \phi_{kl} \int_{-\infty}^{\infty} r_{kl} \, \tau \, dv + B_{kl}}{\frac{1}{K} \sum_{k=1}^{K} \left[n \sin^2 \phi_{kl} \int_{-\infty}^{\infty} r_{kl} \, \tau \, dv + B_{kl} \right]_k}, \tag{3}$$

the resulting ratio Q becomes independent of the constant C. As a caveat, however, by effectively crossing out the number density, the pressure sensitivity of the measurement is significantly reduced.

Possibly caused by Lorentzian wings of the spectral profile of the laser line protruding from the absorption notch of the iodine filter, laser scatter from the rig structure is not completely removed from the measured signal and some laser related background remains. Since the laser frequency is scanned during the measurement, these contributions do not remain constant, but vary with the frequency, which is expressed in Equations (1) and (3) by assigning the index k to the background parameter B. In [34], the laser background is treated by applying a dedicated background correction method that requires the introduction of a regular grid into the light sheet to make the background visible in the resulting dark areas. Since a grid image has to be acquired in addition to a regular image at each scanning frequency, this method effectively doubles the measurement time and is therefore not well suited for application-oriented testing. To tackle the frequency dependence of the background in this work, a first order correction is applied by assigning individual background parameters to the left ($B_{l,1}$ for $v_0 < 18788.4$ cm^{-1}) and the right ($B_{l,2}$ for $v_0 > 18788.4$ cm^{-1}) minimum of the iodine transmission spectrum, Figure 8. When evaluating the flow measurement data, the resulting twelve background parameters must be determined for each resolution element in addition to the five desired flow variables, which is achieved by a fitting Equation (3) using a Levenberg-Marquardt algorithm [34].

D. Use of S-PIV for FRS data benchmark

Stereo Particle Image Velocimetry (S-PIV) has been employed as a benchmarking tool for assessing the FRS measurement system. A pair of CMOS cameras with a resolution of 1280 x 800 px was used for imaging the S-duct outlet plane (0.0 D_out) through the optical walls of the S-duct diffuser. These captured the 3D displacement of DEHS seeding particle with 1 μm average diameter which were illuminated by a pulsed Nd:YAG laser. A dataset comprising 20,000 velocity flow-fields was captured at 8 kHz, and subsequently was time-averaged for comparative assessments with FRS measurements. The S-PIV measurements yielded a spatial resolution at 2.3 x 2.3 mm (0.0144 D_{AIP}), which resulted in approximately 3,000 3D velocity vectors. To mitigate errors stemming from alignment discrepancies between the calibration plate and laser light, a disparity correction technique was employed. This reduced errors to sub-pixel scale. The data has been processed with the commercial software *LaVision Davis ver. 10.2.1.* After processing, only 90% of the AIP radius were considered to eliminate spurious velocity vectors induced by laser light reflections in the optical domain. The uncertainty associated with the velocity components was determined to be 3.3% of the area-averaged, time-averaged streamwise velocity at the AIP, following the methodology proposed by Raffel et al. [35]. Cameras have been installed in a stereo configuration on an optical bench which was integral to the CCITF inlet section (Figure 12a). Due to the reduced space available around the port side of the S-duct intake due to the first bend, the port side camera has been lowered relative to the S-duct centreline (camera in the bottom of the picture, Figure 12b). This allowed to contain the half-stereo angle at acceptable levels. The laser illuminated the AIP through a series of enclosed lightsheet optics from above (Figure 12b).
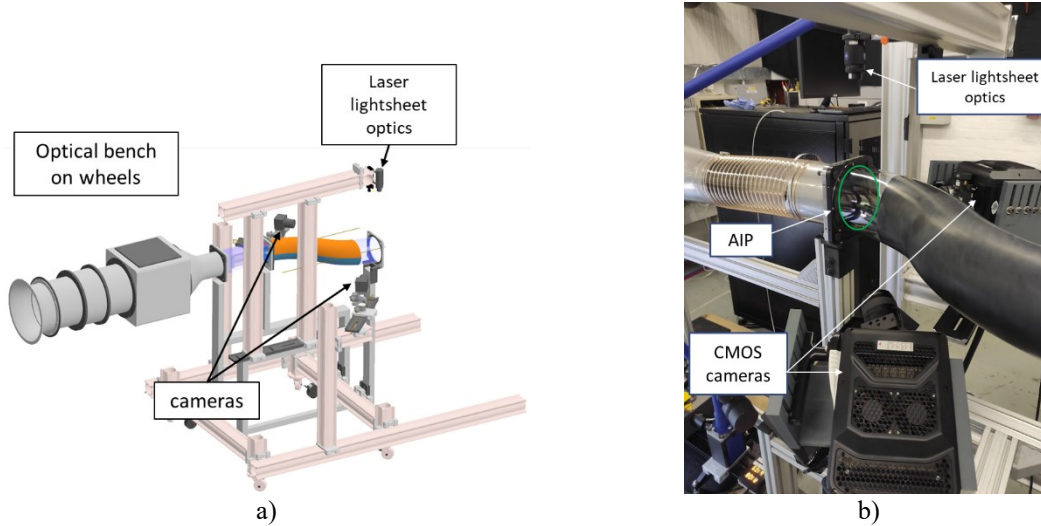
Figure 12: Integration of the PIV instrumentation on the CCITF: a) installation of the cameras and laser lightsheet optics on an optical bench; b) line of sight of the PIV cameras through the optical section of the S-duct intake.

IV.   Flow distortion measurements

### A. Effect of background correction and number of views on FRS results

As discussed in section III, the processing of the FRS data had to account for changing background conditions between reference and flow measurements. This necessity is exemplified by comparing the relative residuals of FRS data fits resulting from a conventional evaluation with C and B derived from the reference measurement (Figure 13 left), and processing involving normalisation of the flow data and background fitting (Figure 13 right). The quality of the FRS data fit is significantly better with the modified evaluation scheme, whereby the values in the centre of the duct are twice as low, and become several factors lower near the channel boundaries. Additionally, the circle-shaped artefacts related to the projections of the laser flange edges cause areas of very high residuals in Figure 13 left, which are significantly improved when fitting the background parameters.
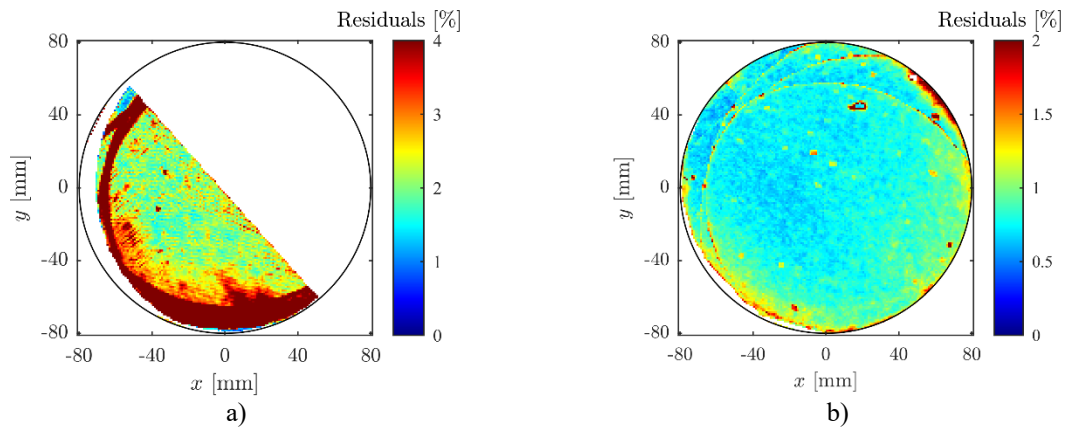
Figure 13: Relative residuals from an FRS flow data fit with a) C_l, $B_{l,1}$ and $B_{l,2}$ derived from a reference measurement, and b) with normalising and fitting $B_{l,1}$ and $B_{l,2}$ for each resolution element.

When combining the frequency scanning technique with a multiple view detection arrangement, a minimal number of three perspectives should in theory be sufficient to determine the five flow variables. Considering the overlap of the camera views in Figure 10b, this criterion is fulfilled for almost the total cross section. During the data processing, the number views that are included per resolution element is dynamically selected based on this map. This means that in certain areas close to the channel boundaries, only three perspectives are used to determine the flow parameters, while others combine four, five or six views.

The effect that the number of perspective views being included in the FRS data processing has on the quality of the results is illustrated in Figure 14. When setting the limit to three views (left column), velocity, pressure and temperature maps cover almost the complete AIP. However, the result areas determined from three perspectives only in the top part close to the channel boundaries contain a lot of spurious vectors and erroneous axial velocity contours. Also, pressure and temperature results appear to be affected. By increasing the minimal number of views to five (middle column), these compromised areas almost completely disappear. Finally, when confining the results to six perspectives (right column) shows the best quality results only, but at the expense of significantly less coverage of the channel cross section. Even though three views should be sufficient in theory, raising the number beyond that minimum seems to improve the measurement's resilience against bias error. In the following, results using a minimum of five perspectives are presented, which can be considered a good compromise between loss of information and quality of results.
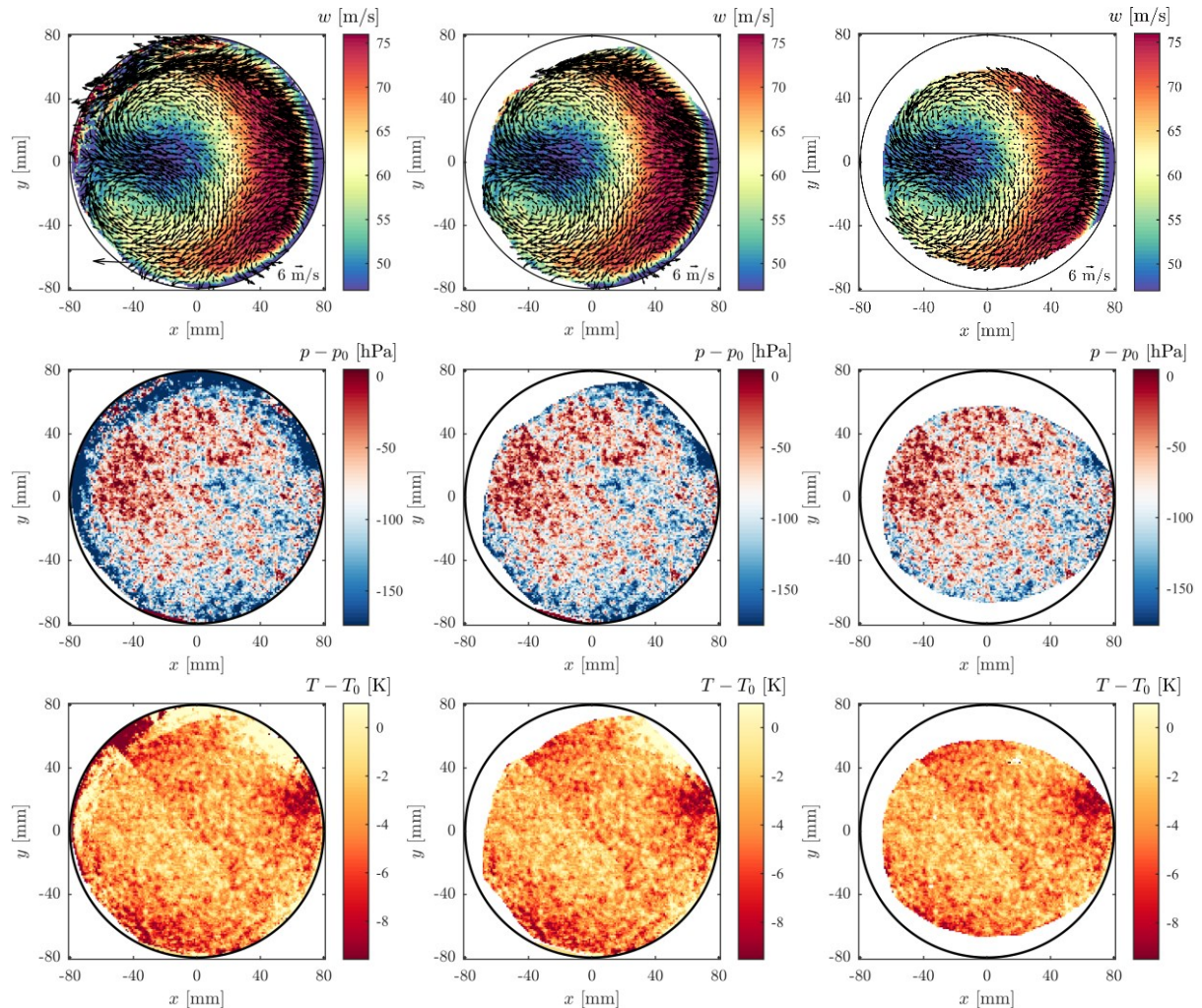

Figure 14: Velocity (top, vectors show u and v components), pressure (middle) and temperature (bottom) fields from FRS using a minimum of 3 (left), 5 (middle) and 6 (right) camera perspectives for $M_{inlet} = 0.27$. Measurements of pressure and temperature are offset by the ambient pressure and temperature conditions, respectively.

B. Benchmark of FRS flow distortion measurements with S-PIV

The analysis of the results for a range of operating points of the CCITF shows a remarkable agreement with the expected topology of the 3D velocity field of this S-duct intake (Figure 15). The velocity maps clearly show the development of the secondary flows and the typical distribution with areas of high-momentum and low-momentum flow distributed in the plane of the S-duct offset bend. This is aligned with the distribution of velocity obtained with S-PIV on the same geometry. In the distribution of the V_Z component measured with FRS, a slight

merging artifact can be seen between the top-right side and bottom-left side of the domain due to the translation of the laser lightsheet to cover full AIP measurements in two takes (Figure 6c). Relative to the combined perspective of 6 views (Figure 9b), only areas with line of sight to 5 views was considered for the final measurements (Figure 15). Additional areas near the top right AIP boundary have been masked due to residual laser light reflections. Nevertheless, FRS measurement allows to perform measurements very close to the AIP boundaries compared to S-PIV, where typically the data near the boundaries is not available due to the laser reflections of the optical domains. This is partially attributed to the advantages of using a bespoke flange for the FRS laser integration, which suppresses the reflections at the boundary walls. In this configuration, the resolution of the FRS data is approximately 1.0 mm in both directions at the AIP (Figure 16). This is superior to the S-PIV data obtained with high-bandwidth cameras, whose measurement resolution is about 2.3 mm. However, it is envisaged that the resolution of FRS data would be comparable to the one obtained with low-bandwidth S-PIV cameras, which offer better spatial resolution compared to high-bandwidth ones. Nevertheless, as discussed, the FRS system enables to perform non-intrusive measurements without the need of seeding particles or high-quality optical access, which can address challenges in measuring flows in embedded systems and in environments where use of seeding is not a viable option [9].
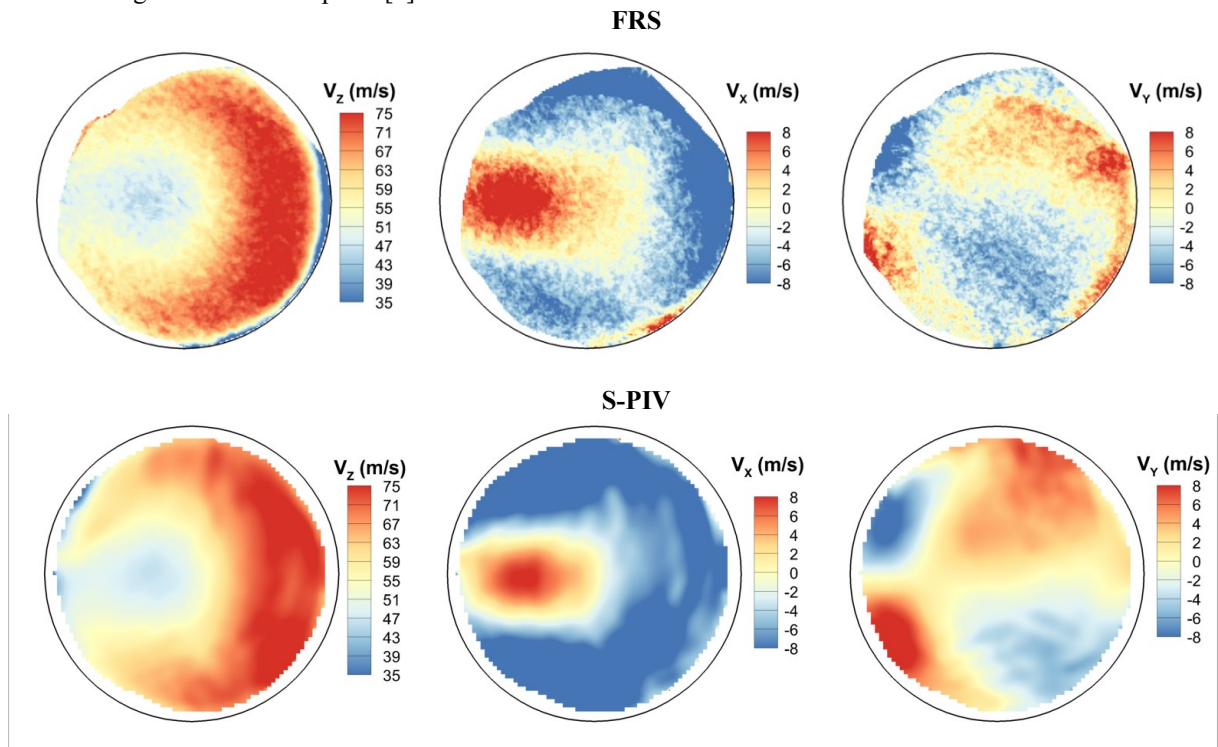
Figure 15: Time-averaged distribution maps of the 3D velocity field measured by FRS at the AIP of the CCITF for M_{inlet} = 0.27 (top). Time-averaged distribution maps of the 3D velocity field measured by PIV at the AIP of the CCITF for M_inlet = 0.27 (bottom).The averaging is done for 20'000 timesteps for PIV.
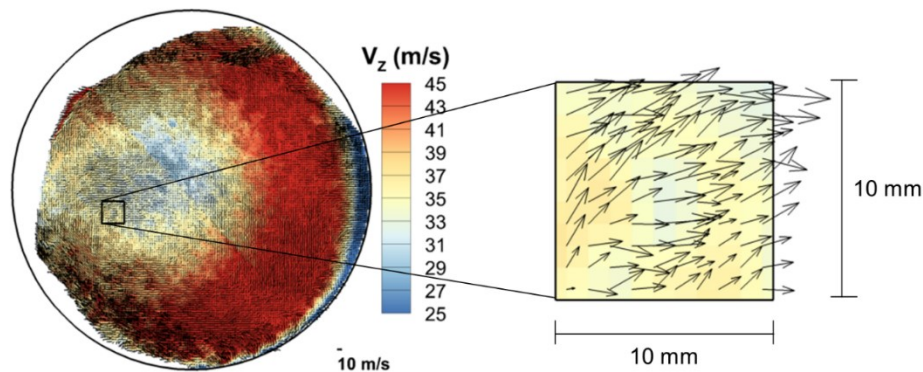
Figure 16: AIP vectors illustrating the resolution of FRS measurements.

V. Conclusions

The current work presented an application of Filtered Rayleigh Scattering (FRS) to measure inlet flow distortion characteristics of an S-duct diffuser in a lab-scale environment. The aim was to demonstrate the FRS t capability by highlighting aspects around the integration of the optical system, data acquisition, data processing and ways to address challenges on the application of the FRS on complex flow fields. The results show that the traditional way of modelling the background with a reference measurement is not sufficient to remove measurement errors which arise due to varying background conditions in more challenging testing environments. In these cases, the introduction of an intensity normalization and the fitting of a background model was reduced the residual error of the measurements. However, while this had a positive impact on velocity measurements, the sensitivity to pressure and temperature variations was substantially reduced. It was also demonstrated that the availability of multiple views achieved with a fibre-bundle camera system can improve the resilience of the measurement system to bias error. These considerations will provide valuable guidelines for the further development of this technique for advanced non-intrusive experimental measurements and a step forward in the path to develop this technique to achieve higher technology readiness levels.

The FRS velocity measurements showed a remarkable agreement with the ones obtained with Stereo-Particle Image Velocimetry (S-PIV). The spatial resolution of the FRS data was comparable to the S-PIV, with the additional advantage of not requiring seeding particles. This technique offers a novel method to measure pressure, temperature with high resolution and synchronously across the measurement plane with a single measurement system. The results indicate very promising potential to assess flows with non-uniform distributions and can improve the understanding of combined flow distortion types, whose interactions are not yet understood.

Acknowledgments

References

[1] ACARE. Flightpath 2050, Europe's Vision for Aviation. Luxembourg: Publications Office of the European Union; 2012. https://doi.org/10.2777/50266.

[2] Bergero C, Gosnell G, Gielen D, Kang S, Bazilian M, Davis SJ. Pathways to net-zero emissions from aviation. Nat Sustain 2023;6:404–14. https://doi.org/10.1038/s41893-022-01046-9.

[3] Hoelzen J, Silberhorn D, Zill T, Bensmann B, Hanke-Rauschenbach R. Hydrogen-powered aviation and its reliance on green hydrogen infrastructure – Review and research gaps. International Journal of Hydrogen Energy 2022;47:3108–30. https://doi.org/10.1016/j.ijhydene.2021.10.239.

[4] Bijewitz J, Seitz A, Hornung M, Luftfahrt B. A review of recent aircraft concepts employing synergistic propulsion-airframe integration, 2016.

[5] Moirou NGM, Sanders DS, Laskaridis P. Advancements and prospects of boundary layer ingestion propulsion concepts. Progress in Aerospace Sciences 2023;138:100897. https://doi.org/10.1016/j.paerosci.2023.100897.

[6] Sahoo S, Zhao X, Kyprianidis K. A Review of Concepts, Benefits, and Challenges for Future Electrical Propulsion-Based Aircraft. Aerospace 2020;7:44. https://doi.org/10.3390/aerospace7040044.

[7] Lee J, Lee S, Cho J. Effect of Inlet Boundary Layer Suction on Flow Distortion in Subsonic Diffusing S-Duct. International Journal of Aeronautical and Space Sciences 2019;20:850–7. https://doi.org/10.1007/s42405-019-00175-4.

[8] Berens TM, Delot A-L, Tormalm MH, Ruiz-Calavera LP, Funes-Sebastian DE, Rein M, et al. Numerical and Experimental Investigations on Highly Integrated Subsonic Air Intakes. 52nd Aerospace Sciences Meeting, Reston, Virginia: 2014-0722, AIAA; 2014. https://doi.org/10.2514/6.2014-0722.

[9] Doll U, Migliorini M, Baikie J, Zachos PK, Röhle I, Melnikov S, et al. Non-intrusive flow diagnostics for unsteady inlet flow distortion measurements in novel aircraft architectures. Progress in Aerospace Sciences 2022;130:100810. https://doi.org/10.1016/j.paerosci.2022.100810.

[10] Gil-Prieto D, Zachos PK, MacManus DG, McLelland G. Unsteady Characteristics of S-duct Intake Flow Distortion. Aerospace Science and Technology 2019;84:938–52. https://doi.org/10.1016/j.ast.2018.10.020.

[11] Migliorini M, Zachos PK, MacManus DG. Novel Method for Evaluating Intake Unsteady Flow Distortion. Journal of Propulsion and Power 2021:1–13. https://doi.org/10.2514/1.B38127.

[12] McLelland G, MacManus DG, Zachos PK, Gil-Prieto D, Migliorini M. Influence of Upstream Total Pressure Profiles on S-Duct Intake Flow Distortion. Journal of Propulsion and Power 2020;36:346–56. https://doi.org/10.2514/1.B37554.

[13] Zachos PK, MacManus DG, Prieto DG, Chiereghin N. Flow Distortion Measurements in Convoluted Aeroengine Intakes. AIAA Journal 2016;54:2819–32. https://doi.org/10.2514/1.J054904.

[14] Röhle, I. Laser Doppler Velocimetry auf der Basis frequenzselektierter Absorption: Aufbau und Einsatz eines Doppler Global Velocimeters. Ph. D. Dissertation. DLR-Forschungsbericht, 1999.

[15] Zachos PK, Frascella M, MacManus DG, Gil-Prieto D. Pressure Flowfield and Inlet Flow Distortion Metrics Reconstruction from Velocity Data. AIAA Journal 2017;55:2929–41. https://doi.org/10.2514/1.J055585.

[16] A Methodology for Assessing Inlet Swirl Distortion. Warrendale, PA: Aerospace Information Report AIR 5686, Society of Automotive Engineers; 2017. https://doi.org/10.4271/AIR5686.

[17] Gas Turbine Engine Inlet Flow Distortion Guidelines. Warrendale, PA: Aerospace Recommended Practice ARP1420C, Society of Automotive Engineers; 2017.

[18] Miles R, Lempert W. Two-dimensional measurement of density, velocity, and temperature in turbulent high-speed air flows by UV rayleigh scattering. Appl Phys B 1990;51:1–7. https://doi.org/10.1007/BF00332317.

[19] Forkey JN, Finkelstein ND, Lempert WR, Miles RB. Demonstration and characterization of filtered Rayleigh scattering for planar velocity measurements. AIAA Journal 1996;34:442–8. https://doi.org/10.2514/3.13087.

[20] Doll U, Stockhausen G, Willert C. Endoscopic filtered Rayleigh scattering for the analysis of ducted gas flows. Experiments in Fluids 2014;55:1690. https://doi.org/10.1007/s00348-014-1690-z.

[21] Doll U, Röhle I, Dues M, Kapulla R. Time-resolved multi-parameter flow diagnostics by filtered Rayleigh scattering: system design through multi-objective optimisation. Meas Sci Technol 2022;33:105204. https://doi.org/10.1088/1361-6501/ac7cca.

[22] Doll U, Kapulla R, Steinbock J, Dues M, Migliorini M, Zachos PK. Seeding-free inlet flow distortion measurement by filtered Rayleigh scattering: diagnostic approach and verification. AIAA SCITECH 2023 Forum, National Harbor, MD & Online: American Institute of Aeronautics and Astronautics; 2023. https://doi.org/10.2514/6.2023-1372.

[23] Doll U, Kapulla R, Dues M, Steinbock J, Melnikov S, Röhle I, et al. Towards time-resolved multi-property measurements by filtered Rayleigh scattering: diagnostic approach and verification. PREPRINT (Version 1) Available at Research Square, Accepted for Publication in Experiments in Fluids 2023. https://doi.org/10.21203/rs.3.rs-3233271/v1.

[24] Migliorini M, Zachos PK, MacManus DG, Haladuda P. S-duct flow distortion with non-uniform inlet conditions. Proceedings of the Institution of Mechanical Engineers, Part G: Journal of Aerospace Engineering 2022:095441002211016. https://doi.org/10.1177/09544100221101669.

[25] Gil-Prieto D. Unsteady Flow Distortion in Complex Aero-Engine Intakes. PhD Thesis. Propulsion Engineering Centre, School of Aerospace, Transport and Manufacturing, Cranfield University, 2018.

[26] Tanguy G, MacManus DG, Garnier E, Martin PG. Characteristics of unsteady total pressure distortion for a complex aero-engine intake duct. Aerospace Science and Technology 2018;78:297–311. https://doi.org/10.1016/j.ast.2018.04.031.

[27] Gil-Prieto D, MacManus DG, Zachos PK, Tanguy G, Menzies KR. Convoluted Intake Distortion Measurements Using Stereo Particle Image Velocimetry. AIAA Journal 2017;55:1878–92. https://doi.org/10.2514/1.J055467.

[28] MacManus DG, Chiereghin N, Prieto DG, Zachos P. Complex Aeroengine Intake Ducts and Dynamic Distortion. AIAA Journal 2017;55:2395–409. https://doi.org/10.2514/1.J054905.

[29] Tanguy G, MacManus DG, Zachos P, Gil-Prieto D, Garnier E. Passive Flow Control Study in an S-Duct Using Stereo Particle Image Velocimetry. AIAA Journal 2017;55:1862–77. https://doi.org/10.2514/1.J055354.

[30] Garnier E. Flow Control by Pulsed Jet in a Curved S-Duct: A Spectral Analysis. AIAA Journal 2015;53:2813–27. https://doi.org/10.2514/1.J053422.

[31] Doll U, Stockhausen G, Willert C. Pressure, temperature, and three-component velocity fields by filtered Rayleigh scattering velocimetry. Optics Letters 2017;42:3773–6. https://doi.org/10.1364/OL.42.003773.

[32] Bradski G. The OpenCV Library. Dr Dobb's Journal of Software Tools 2000;120:122–5.

[33] Miles RB, Lempert WR, Forkey JN. Laser Rayleigh scattering. Meas Sci Technol 2001;12:R33–51. https://doi.org/10.1088/0957-0233/12/5/201.

[34] Doll U, Burow E, Stockhausen G, Willert C. Methods to improve pressure, temperature and velocity accuracies of filtered Rayleigh scattering measurements in gaseous flows. Measurement Science and Technology 2016;27:125204. https://doi.org/10.1088/0957-0233/27/12/125204.

[35] Raffel M, Willert CE, Wereley ST, Kompenhans J, Willert S, Wereley ST, et al. Particle Image Velocimetry: A Practical Guide. In: Springer-Verlag, editor. Particle Image Velocimetry. 2nd ed., Berlin: Springer; 2007, p. 203–41.